High-Harmonic Generation in Plasmonically Enhanced Bicircular Fields

A First-Principles Formal Report

June 2026

Abstract

This report presents a formal account of high-harmonic generation (HHG) in bichromatic counter-rotating circularly polarised fields with spatially inhomogeneous plasmonic enhancement. The treatment is organised from first principles. We begin with the single-active-electron time-dependent Schrödinger equation in the length gauge, identify the microscopic dipole observable from which the harmonic spectrum is obtained, and then derive the semiclassical recollision picture as the stationary-phase limit of strong-field theory. That framework is used to explain the standard cutoff law $E_{\text{cut}} \approx I_p + 3.17U_p$, the role of return trajectories, and the separation into short and long branches.

The bicircular driving field is then analysed as a dynamical-symmetry problem. Its combined temporal and spatial threefold symmetry explains why the homogeneous response organises naturally into three ionisation lobes and, at the level of emitted harmonics, supports the familiar $3q\pm1$ channels while suppressing the $3q$ orders. Against that homogeneous reference, we examine two models of plasmonic enhancement: a local linear expansion and a dipole-like inverse-cubic field associated with a nearby nanosphere. Their equations of motion are derived explicitly and their physical admissibility is compared.

The figure set is restricted to traceable scientific figures rather than presentation art. The report therefore uses the homogeneous and enhanced return-time maps documented in Bray's thesis, together with published figures illustrating field inhomogeneity and plasmonically extended harmonic cutoffs. The central conclusion is that the cubic near-field model is the only one of the two enhancement models that remains physically credible over the excursion range relevant to the reported trajectories. It preserves the bicircular threefold structure while selectively suppressing and reshaping recollision channels in a manner consistent with a realistic nanoscale near field.

1 Introduction

High-harmonic generation is a non-perturbative strong-field process in which an atom or molecule driven by an intense optical field emits coherent radiation at frequencies far above the driving frequency [1, 2]. The phenomenon is important not merely as a nonlinear-optics curiosity but because it provides a route from near-infrared or mid-infrared driving fields to coherent extreme-ultraviolet emission and attosecond temporal structure. Any serious analysis of HHG must therefore keep two levels of description in view simultaneously: a microscopic description in terms of laser-driven electronic dynamics, and a spectral description in terms of the radiation emitted upon recombination.

The present report concerns a specific version of that problem: HHG in a bichromatic counter-rotating circularly polarised field, modified by a spatially varying plasmonic enhancement. This is a more structured system than the textbook linearly polarised case. In linear polarisation, the field reverses along a single axis and naturally supports recollision. In circular polarisation, by contrast, the electron is usually driven away from the ion and ordinary recollision is strongly suppressed. A bicircular field avoids that simple dichotomy. Because it superposes two circular components of frequencies ω and 2ω rotating in opposite senses, the resulting field possesses a discrete rotational symmetry rather than a continuous one, and that symmetry strongly constrains both the allowed return trajectories and the emitted harmonic channels [3–5].

The plasmonic component adds a second layer of structure. Near a metallic nanostructure, the local electric field can be enhanced and, crucially, spatially inhomogeneous on the scale of the electron excursion. That means the continuum electron no longer sees a purely time-dependent driving field. Instead its dynamics become genuinely spatiotemporal. Because harmonic emission depends sensitively on the electron's return energy and return time, even a modest spatial variation in the local field can change which trajectories survive, which are suppressed, and how the return landscape is redistributed [6–8].

The immediate aim of this report is therefore narrow but substantial: to rewrite the project material in a form appropriate to a graduate-level physics report. That requires three upgrades relative to a presentation script. First, the field equations and spectral observables must be defined explicitly. Second, the bicircular and plasmonic models must be justified mathematically rather than only described qualitatively. Third, the figures must be treated as scientific evidence with clear provenance, not as illustrative slide components. The discussion that follows is built to meet those requirements.

2 Microscopic Formulation

2.1 Single-active-electron description

We begin with the single-active-electron approximation, in which one electron is treated dynamically and the remaining electrons enter only through an effective binding potential. In the length gauge, and in atomic units unless stated otherwise, the time-dependent Schrödinger equation is

$$i\frac{\partial}{\partial t}\Psi(\boldsymbol{r},t) = \left[-\frac{1}{2}\nabla^2 + V(\boldsymbol{r}) + \boldsymbol{r}\cdot\boldsymbol{E}(\boldsymbol{r},t)\right]\Psi(\boldsymbol{r},t). \tag{1}$$

Here $V(\boldsymbol{r})$ is the effective binding potential, $\Psi(\boldsymbol{r},t)$ is the electronic wavefunction, and $\boldsymbol{E}(\boldsymbol{r},t)$ is the laser field. In the homogeneous approximation one writes $\boldsymbol{E}(\boldsymbol{r},t) = \boldsymbol{E}(t)$, while in the plasmonic case the spatial dependence must be retained.

The harmonic spectrum is extracted from a dipole observable. Depending on the numerical method, one may use the dipole moment, dipole velocity, or dipole acceleration. A convenient formal expression is

$$S(\Omega) \propto \left| \int_{-\infty}^{\infty} \mathrm{d}t \, e^{i\Omega t} \, \ddot{\boldsymbol{d}}(t) \right|^2, \qquad \boldsymbol{d}(t) = \langle \Psi(t) | \boldsymbol{r} | \Psi(t) \rangle \,. \tag{2}$$

This equation makes the basic point with full clarity: harmonic emission is determined by the time-dependent acceleration of the electronic dipole. In a trajectory language, recombination events imprint themselves on $\ddot{\boldsymbol{d}}(t)$ as bursts of high-frequency radiation.

2.2 Strong-field approximation and semiclassical action

The formal route from equation (1) to the semiclassical three-step picture is provided by strong-field theory [2]. In that framework the continuum motion is approximated by Volkov propagation in the laser field, while the binding potential is retained at ionisation and recombination. The dipole can then be written schematically as an integral over ionisation time t', recombination time t, and intermediate canonical momentum $\boldsymbol{p}$:

$$\boldsymbol{d}(t) \sim \int_{-\infty}^{t} \mathrm{d}t' \int \mathrm{d}^3 p \; \boldsymbol{d}_{\mathrm{rec}}[\boldsymbol{p} + \boldsymbol{A}(t)] \; a_{\mathrm{ion}}[\boldsymbol{p} + \boldsymbol{A}(t')] \exp[-iS(\boldsymbol{p}, t, t')] + \text{c.c.}, \tag{3}$$

where $\boldsymbol{A}(t)$ is the vector potential, $\boldsymbol{E}(t) = -\partial_t \boldsymbol{A}(t)$, and

$$S(\boldsymbol{p}, t, t') = \int_{t'}^{t} \left[\frac{1}{2} \left(\boldsymbol{p} + \boldsymbol{A}(\tau) \right)^2 + I_p \right] \mathrm{d}\tau \tag{4}$$

is the semiclassical action. The saddle-point conditions

$$\partial_{\boldsymbol{p}} S = 0, \tag{5}$$

$$\partial_{t'} S = 0, \tag{6}$$

$$\partial_t S = \Omega \tag{7}$$

have immediate physical meaning. Equation (5) enforces return to the ionic core, (6) is the ionisation condition, and (7) is the recombination energy balance. In this sense the three-step picture is not an independent cartoon added on top of quantum mechanics; it is the stationary-phase structure of the strong-field amplitude itself.

2.3 Recovery of the cutoff law

In the linearly polarised reference problem one may write

$$E(t) = E_0 \cos(\omega t), \qquad A(t) = \frac{E_0}{\omega} \sin(\omega t), \tag{8}$$

and treat the liberated electron classically after ionisation. If the electron is released at time t_i with vanishing initial velocity, the Newton equation $\ddot{x} = -E(t)$ yields

$$\dot{x}(t) = -\frac{E_0}{\omega}\left[\sin(\omega t) - \sin(\omega t_i)\right], \tag{9}$$

$$x(t) - x(t_i) = \frac{E_0}{\omega^2}\left[\cos(\omega t) - \cos(\omega t_i) + \omega(t - t_i)\sin(\omega t_i)\right]. \tag{10}$$

Recollision occurs when $x(t_r) = x(t_i)$. Maximisation of the kinetic energy

$$E_k(t_r) = \frac{1}{2}\dot{x}(t_r)^2 \tag{11}$$

over ionisation and return times gives the well-known result

$$E_{k,\max} = 3.17U_p, \qquad U_p = \frac{E_0^2}{4\omega^2}, \tag{12}$$

and therefore the cutoff law

$$E_{\text{cut}} \approx I_p + 3.17U_p. \tag{13}$$

This is the first essential kinematic scaling law of HHG. It says that the highest accessible harmonic energy is controlled by the binding energy and the laser-induced quiver energy. The rest of the report can be read, in large part, as an analysis of how bicircular symmetry and spatial inhomogeneity modify the route by which the electron samples that quiver energy and returns to the core.

3 Bicircular Driving Field and Dynamical Symmetry

3.1 Field definition

The driving field used throughout the project is a bichromatic counter-rotating circularly polarised field of the form

$$\boldsymbol{E}_{\text{bc}}(t) = E_0 g(t)\begin{pmatrix}\cos(\omega t) + \cos(2\omega t)\\ \sin(\omega t) - \sin(2\omega t)\end{pmatrix}, \tag{14}$$

with envelope $g(t)$. In the project material the fundamental frequency is $\omega = 0.05$ a.u., corresponding to a wavelength of approximately 900 nm, with a neon target model of ionisation potential $I_p = 0.793$ a.u. [9, 10]. The second colour at 2ω then corresponds to 450 nm.

Unlike a linearly polarised field, equation (14) is not confined to a single axis. Unlike a single-colour circular field, however, it does not exhibit full rotational drift. Its structure is discrete and threefold. The electron therefore experiences a field with preferred launch windows rather than a continuous angular sweep.

3.2 Threefold symmetry

The bicircular field obeys the dynamical-symmetry relation

$$\boldsymbol{E}_{\mathrm{bc}}\left(t+\frac{T}{3}\right)=R\left(\frac{2\pi}{3}\right)\boldsymbol{E}_{\mathrm{bc}}(t), \qquad T=\frac{2\pi}{\omega}, \tag{15}$$

where $R(2\pi/3)$ is a planar rotation by 120°. This can be verified directly by substituting $t \mapsto t+T/3$ into equation (14) and using the periodicity of the trigonometric functions. Equation (15) means that a time translation by one third of the fundamental period is equivalent to a spatial rotation by $2\pi/3$.

At the level of the emitted dipole, the same symmetry implies

$$\boldsymbol{d}\left(t+\frac{T}{3}\right)=R\left(\frac{2\pi}{3}\right)\boldsymbol{d}(t). \tag{16}$$

Writing the circular components $d_\pm(t)=d_x(t)\pm i d_y(t)$, one finds

$$d_\pm\left(t+\frac{T}{3}\right)=e^{\pm i2\pi/3}d_\pm(t). \tag{17}$$

Fourier expansion then gives the selection rule

$$e^{-i\Omega T/3}=e^{\pm i2\pi/3}, \tag{18}$$

so that only harmonics satisfying

$$\Omega=(3q\pm 1)\omega \tag{19}$$

survive, while the $3q$ orders are symmetry forbidden [3–5]. This result is central because it shows that the spectral sparsity of bicircular HHG is not a numerical accident. It is required by the discrete space-time symmetry of the driver.

3.3 Return-time interpretation

The same symmetry is visible in trajectory space. If one plots return time against harmonic order, the homogeneous bicircular case naturally separates into three coloured lobes corresponding to the three launch sectors within one optical period. The harmonic order associated with a returning electron is

$$n=\frac{I_p+E_k(t_r)}{\omega}, \tag{20}$$

which is the project's preferred return-map variable [10]. This equation is simply the photon-energy balance written in units of the fundamental quantum ω. It therefore translates return kinematics into a directly spectral quantity.

Figure 1 is therefore not a decorative warm-up plot. It is the baseline against which the plasmonically enhanced cases must be judged. The periodicity at one-third-cycle intervals is the clearest trajectory-space manifestation of the underlying C_3 symmetry.

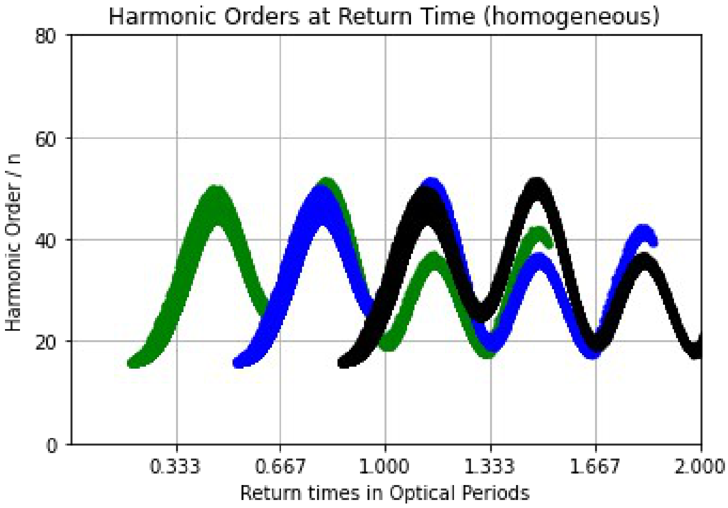

Figure 1: Homogeneous bicircular reference case, showing harmonic order versus return time for the three ionisation lobes of the driving field. The threefold periodic structure follows directly from the dynamical symmetry of the bicircular driver. Source: Bray thesis, Fig. 8.4 [10].

4 Plasmonic Enhancement as a Spatially Inhomogeneous Field

4.1 Why a spatial model is required

In conventional gas-phase HHG modelling, the driving field is often taken to be homogeneous across the electron excursion. Near a metallic nanostructure that assumption breaks down. The local field enhancement is strongest near the structure and decays over nanometre scales, so the electron samples different field strengths along its trajectory. At that point the force law must be written as

$$\ddot{\boldsymbol{r}}(t) = -\boldsymbol{E}_{\rm tot}(\boldsymbol{r}, t), \qquad \boldsymbol{E}_{\rm tot}(\boldsymbol{r}, t) = \boldsymbol{E}_{\rm bc}(t) + \boldsymbol{E}_{\rm pl}(\boldsymbol{r}, t), \tag{21}$$

and the continuum action is no longer purely Volkov-like.

The immediate physical effect is easy to state. Because U_p scales like E^2, a local enhancement changes the quiver energy. Because the enhancement is position dependent, it also changes the force differently on different branches of the trajectory. Consequently the recollision landscape is not merely shifted but selectively reshaped.

4.2 Local linear model

The simplest spatial model is a linear expansion about a reference point:

$$\boldsymbol{E}_{\rm pl}^{(\rm lin)}(\boldsymbol{r}, t) = E_0 g(t) \begin{pmatrix} \beta_x x E_x(t) \\ \beta_y y E_y(t) \end{pmatrix}, \tag{22}$$

where β_x and β_y parameterise the strength of the inhomogeneity along the corresponding Cartesian directions [10]. In component form, the equations of motion become

$$\ddot{x}(t) = -E_x(t)\,[1 + \beta_x x(t)]\,, \tag{23}$$

$$\ddot{y}(t) = -E_y(t)\,[1 + \beta_y y(t)]\,. \tag{24}$$

Mathematically, equations (23) and (24) are appealing because they are the first nontrivial correction to the homogeneous field. Physically, however, they are only local approximations. Once the electron excursion is large enough that $\beta_x x$ or $\beta_y y$ ceases to be small, the field can change sign or grow in a way that is no longer representative of a real near field. This limitation is not cosmetic; it is exactly why some linear-model trajectories can become physically suspect.

4.3 Dipole-like inverse-cubic model

A more realistic plasmonic model ties the local field to a nanosphere-induced dipole field. In the project material this is represented as an inverse-cubic dependence,

$$\boldsymbol{E}_{\mathrm{pl}}^{(\mathrm{cub})}(\boldsymbol{r}, t) = \frac{3\hat{\boldsymbol{r}}_{\mathrm{se}}\,(\hat{\boldsymbol{r}}_{\mathrm{se}} \cdot \boldsymbol{d}(t)) - \boldsymbol{d}(t)}{r_{\mathrm{se}}^3}, \qquad \boldsymbol{d}(t) = \delta\,\boldsymbol{E}_{\mathrm{bc}}(t), \tag{25}$$

where $\boldsymbol{r}_{\mathrm{se}}$ is the electron position relative to the nanosphere centre and δ is a proportionality constant relating the induced dipole to the driving field [8, 10]. The essential point is that the enhancement now follows an actual near-field geometry: it decays with distance, it has a directional structure fixed by the induced dipole, and it does not continue as a globally valid straight-line approximation.

Figure 2 distils the model comparison to its physical core. The linear model is not wrong because it is simple; it is wrong when it is used outside the narrow region in which linearisation is valid. The inverse-cubic model is therefore not merely a more elaborate fit. It is the first model in the project that carries a defensible geometric interpretation.

4.4 Cutoff extension and plasmonic motivation

Before turning to the Bray return-time maps, it is useful to recall why plasmonic enhancement is interesting at all. If the local field amplitude is increased, then the local quiver energy increases and the cutoff can move to higher harmonic orders. Published plasmonic-HHG calculations indeed show such an extension of the spectral plateau and cutoff [6, 11].

The purpose of figure 3 in this report is limited but important. It establishes that plasmonic inhomogeneity is not introduced here as a formal perturbation with no observable consequence. It is introduced because a modified local field can change the accessible harmonic range and the recollision energy budget in a measurable way.

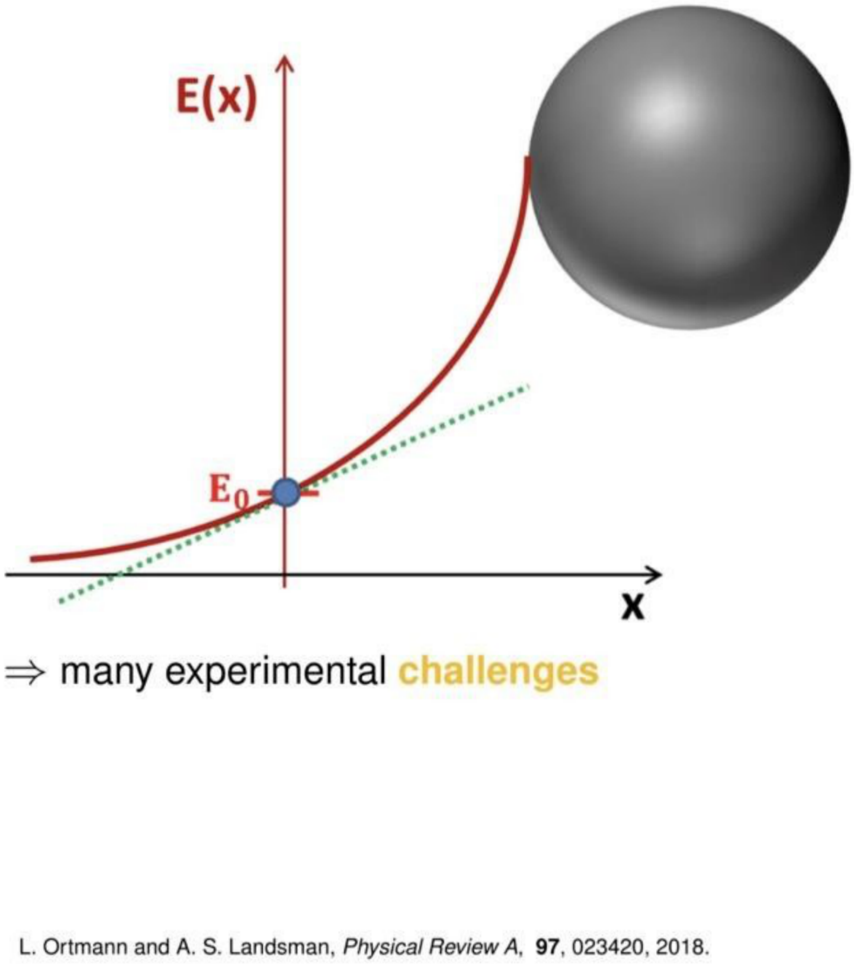

Figure 2: Published schematic illustrating why a linear expansion is only a local approximation to the true near-field profile around a nanostructure. The solid curve represents the nonlinear field profile, while the dotted line indicates its local linearisation about a chosen point. Source: adapted slide reproduction of Ortmann and Landsman, *Physical Review A* **97**, 023420 (2018) [8].

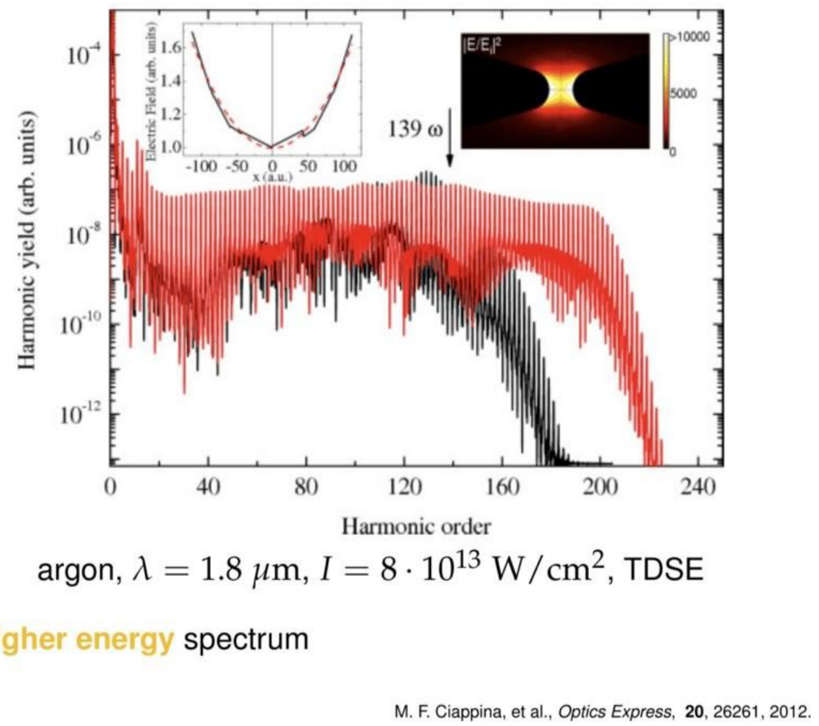

Figure 3: Example of cutoff extension under a plasmonically enhanced driving field. The enhanced-field case reaches substantially higher harmonic order than the homogeneous reference. The slide extraction attributes the figure to Ciappina and collaborators; the corresponding traceable source family is the plasmonic-HHG literature of Shaaran, Ciappina, and Lewenstein [6, 11].

5 Interpretation of the Reported Return-Time Maps

5.1 What the figures represent

The Bray figures used in this report are return-time maps rather than directly measured far-field spectra. Each point corresponds to a recombining trajectory labelled by its ionisation lobe, return time, and inferred harmonic order. These figures therefore visualise the structure of the returning electronic ensemble rather than the full macroscopic XUV yield. This distinction matters because one should not infer phase matching, propagation, or detector-level brightness from these maps alone.

What they do provide, however, is exactly the right information for a microscopic comparison of homogeneous and inhomogeneous driving. They tell us which branches survive, which energies are reached, and how the field geometry redistributes the recollision phase space.

5.2 β_x enhancement

Figure 4 supports several precise conclusions.

First, the threefold periodicity remains visible across all panels. This is nontrivial. It means the plasmonic enhancement deforms the bicircular recollision landscape but does not erase the underlying dynamical symmetry inherited from the optical driver.

Second, the linear model produces increasingly long delayed returns as β_x grows. In the upper-right panel, trajectories appear well beyond one optical cycle after launch. Mathematically, such behaviour is permitted by the linearised force law. Physically, it is much harder to defend. If the field model is extrapolated beyond its domain of validity, the trajectory set can acquire branches that owe more to the approximation than to the nanoscale electrodynamics.

Third, the cubic model produces a different reorganisation from the outset. The lower row is dominated by steep branches with strong short-trajectory character, while the earliest green lobe is more visibly truncated. This is exactly the kind of directional selectivity one expects when the enhancement field is tied to a dipole-like nanosphere geometry rather than to a uniform global slope.

Fourth, the comparison shows that the realistic near field changes not only energy gain but also effective launch geometry. In the cubic case the local field biases certain lobes against return because the enhanced field points away from the core along those branches. The effect is therefore not a scalar amplification. It is a vectorial reshaping of the trajectory space.

5.3 β_y enhancement

The β_y results in figure 5 are, if anything, even more diagnostic.

The first green-lobe return remains prominent across the parameter scan, indicating that one launch sector continues to support prompt high-energy return. By contrast, the blue lobe is progressively suppressed as the enhancement increases, especially in the cubic model. That selective

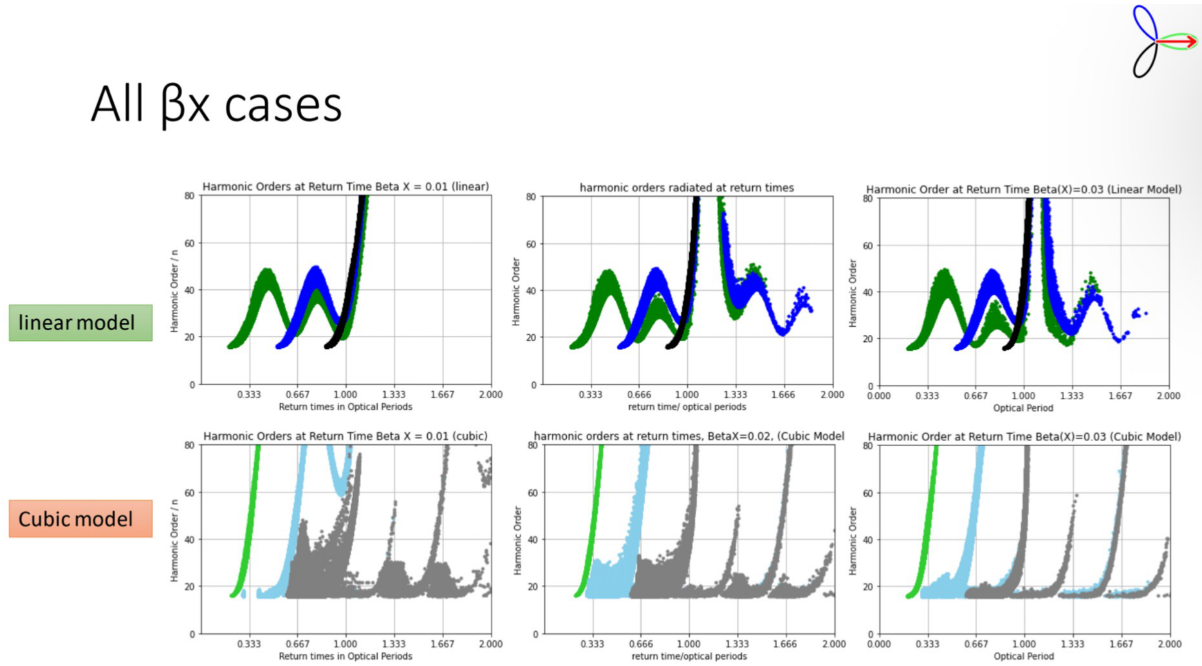

Figure 4: Return-time maps for enhancement along the x direction. The upper row shows the linear model and the lower row the cubic model, for $\beta_x = 0.01$, 0.02, and 0.03 a.u. from left to right. Source: Bray thesis, Fig. 8.6 [10].

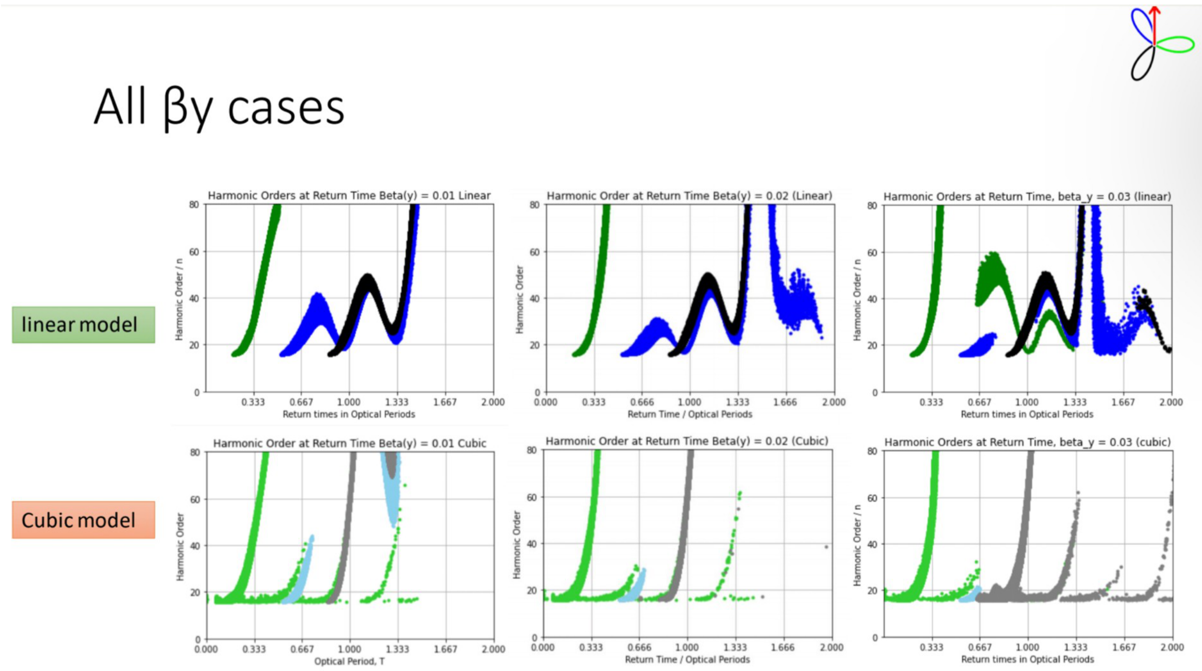

Figure 5: Return-time maps for enhancement along the y direction. The upper row shows the linear model and the lower row the cubic model, for $\beta_y = 0.01$, 0.02, and 0.03 a.u. from left to right. Source: Bray thesis, Fig. 8.7 [10].

depletion is the clearest evidence in the entire figure set that the near field acts anisotropically on the recollision channels.

The same qualitative caution that applied to the β_x linear model applies here as well. The upper-row figures again exhibit very late, sparse return branches whose physical credibility is questionable once the linear field has been extrapolated far from the local expansion point. The lower-row cubic figures, by contrast, remain structured, selective, and geometrically interpretable. They show suppression, truncation, and energy redistribution, but not the same kind of globally proliferating artificial branch structure.

In this sense the β_y case strengthens rather than merely repeats the β_x conclusion. The superiority of the cubic model is not inferred from one especially favourable orientation. It persists under a distinct directional perturbation of the bicircular field.

6 Why the Cubic Model is Physically Preferable

The model comparison can now be stated at a more formal level.

Suppose the field is expanded locally as

$$\boldsymbol{E}(\boldsymbol{r},t) = \boldsymbol{E}(\boldsymbol{0},t) + (\boldsymbol{r}\cdot\nabla)\,\boldsymbol{E}\Big|_{\boldsymbol{0}} + \cdots . \tag{26}$$

Then the linear model retains only the first spatial derivative. That is acceptable provided the characteristic excursion length ℓ satisfies

$$\ell \ll \frac{|\boldsymbol{E}|}{|\nabla \boldsymbol{E}|}, \tag{27}$$

so that higher derivatives are negligible. In a strong-field recollision problem, however, the electron can travel far enough that this condition becomes doubtful. If so, higher-order spatial structure is not optional. It becomes dynamically relevant.

The inverse-cubic near field addresses this by embedding the electron in a field whose spatial variation already reflects the expected nanosphere geometry. It is still a model, of course; it is not a full electrodynamic simulation of a real fabricated structure. But it has the essential qualitative virtues that the linear model lacks:

1. it decays with distance rather than growing indefinitely;
2. it has a definite directional structure tied to the induced dipole;
3. it does not introduce sign changes purely as an artefact of extrapolated linearisation;
4. it reproduces lobe-selective suppression patterns that remain intelligible within the bicircular symmetry framework.

For the purpose of a graduate-level interpretation, that is enough to justify the project's central conclusion: the cubic model is not simply one possible fit among many. It is the first of the two enhancement models that can support physically credible inference over the excursion scales visible in the reported return maps.

7 Limitations and Scope

Two limitations should be stated explicitly.

First, these results concern trajectory-resolved return maps, not complete macroscopic HHG propagation. The figures therefore support conclusions about recollision kinematics, channel suppression, and harmonic-order accessibility, but not by themselves about phase matching, absolute conversion efficiency, or experimentally detected beam profiles.

Second, one of the reused literature figures was recovered from presentation assets rather than from a freshly extracted journal PDF. Its scientific source family is clear, but the exact article-to-figure correspondence should be verified against the original paper before any formal submission that requires archival bibliographic precision. The Bray thesis figures and the Ortmann–Landsman field-shape figure, by contrast, are secure in provenance.

8 Conclusion

This report has reformulated the project in a more formal and self-contained way. Starting from the time-dependent Schrödinger equation, we identified the microscopic dipole observable that generates the HHG spectrum, derived the semiclassical action underlying the three-step picture, and recovered the standard cutoff law $I_p + 3.17U_p$. We then showed that the bicircular ω–2ω driver possesses a discrete threefold dynamical symmetry and that this symmetry governs both the structure of the return-time maps and the harmonic selection rules.

Once plasmonic enhancement is introduced, the problem becomes intrinsically spatiotemporal. The local field no longer only changes the scale of the electron's quiver energy; it changes the geometry of the recollision itself. That is why the field model matters so much. The linear model is useful as a formal local expansion, but it cannot be treated as globally reliable over the relevant trajectory range. The inverse-cubic model, by contrast, remains geometrically meaningful and yields lobe-selective suppression and trajectory restructuring that are physically interpretable.

The scientific judgement that follows is therefore straightforward. Within the scope of the reported figures, the homogeneous bicircular case provides the correct symmetry baseline; the linear enhancement model is mathematically convenient but physically fragile; and the cubic near-field model is the appropriate basis for interpreting plasmonically enhanced HHG in this project. That conclusion is supported both by first-principles reasoning and by the literature figures reproduced here.

References

[1] P. B. Corkum. Plasma perspective on strong-field multiphoton ionization. *Physical Review Letters*, 71(13):1994–1997, 1993. doi: 10.1103/PhysRevLett.71.1994.

[2] M. Lewenstein, Ph. Balcou, M. Yu. Ivanov, Anne L'Huillier, and P. B. Corkum. Theory of high-harmonic generation by low-frequency laser fields. *Physical Review A*, 49(3):2117–2132, 1994. doi: 10.1103/PhysRevA.49.2117.

[3] D. Baykusheva, M. S. Ahsan, N. Lin, and H. J. Wörner. Bicircular high-harmonic spectroscopy reveals dynamical symmetries of atoms and molecules. *Physical Review Letters*, 116(12):123001, 2016. doi: 10.1103/PhysRevLett.116.123001.

[4] D. M. Reich and L. B. Madsen. Illuminating molecular symmetries with bicircular high-order-harmonic generation. *Physical Review Letters*, 117(13):133902, 2016. doi: 10.1103/PhysRevLett.117.133902.

[5] O. Neufeld, D. Podolsky, and O. Cohen. Floquet group theory and its application to selection rules in harmonic generation. *Nature Communications*, 10:405, 2019. doi: 10.1038/s41467-018-07935-y.

[6] T. Shaaran, M. F. Ciappina, and M. Lewenstein. Estimating the plasmonic field enhancement using high-order harmonic generation: The role of inhomogeneity of the fields. *Journal of Modern Optics*, 60(13):1054–1060, 2013. doi: 10.1080/09500340.2012.735267.

[7] C. Zagoya, M. Bonner, H. Chomet, E. Slade, and C. Figueira de Morisson Faria. Different time scales in plasmonically enhanced high-order-harmonic generation. *Physical Review A*, 93(5):053419, 2016. doi: 10.1103/PhysRevA.93.053419.

[8] L. Ortmann and A. S. Landsman. Analysis of the higher-energy structure in strong-field ionization with inhomogeneous electric fields. *Physical Review A*, 97(2):023420, 2018. doi: 10.1103/PhysRevA.97.023420.

[9] Irfana N. Ansari, Cornelia Hofmann, Lukas Medišauskas, Maciej Lewenstein, Marcelo F. Ciappina, and Gopal Dixit. Controlling polarization of attosecond pulses with plasmonic-enhanced bichromatic counter-rotating circularly polarised fields. *Physical Review A*, 103 (1):013104, 2021. doi: 10.1103/PhysRevA.103.013104.

[10] Abbie C. Bray. *Electron Rescattering Picture in a Strong-Field Laser Regime: Diverse Initial State Geometry under Coulomb Influences*. PhD thesis, University College London, 2022. URL `https://discovery.ucl.ac.uk/id/eprint/10157220/`.

[11] M. F. Ciappina, T. Shaaran, and M. Lewenstein. High order harmonic generation in noble gases using plasmonic field enhancement, 2012. URL `https://arxiv.org/abs/1210.5610`.